IEEE Access
Multidisciplinary | Rapid Review | Open Access Journal

Received February 12, 2021, accepted February 20, 2021, date of publication March 1, 2021, date of current version March 11, 2021.

Digital Object Identifier 10.1109/ACCESS.2021.3063016

Control Design and Stability Analysis of Power Converters: The Discrete Generalized Bode Criterion

ANDONI URTASUN, (Senior Member, IEEE), JAVIER SAMANES, (Member, IEEE), ERNESTO L. BARRIOS, (Member, IEEE), AND PABLO SANCHIS, (Senior Member, IEEE)
Department of Electrical, Electronic and Communications Engineering, Public University of Navarre, 31006 Pamplona, Spain

Corresponding author: Andoni Urtasun (andoni.urtasun@unavarra.es)

This work was supported in part by the Agencia Estatal de Investigación (AEI) under Grant PID2019-110956RB-I00/AEI/10.13039/501100011033, and in part by the Ingeteam Power Technology.

ABSTRACT For the controller design and stability analysis of power electronic converters, the Bode stability criterion and its subsequent revisions are the most practical tools. However, even though the control of the power converter is usually implemented in a microprocessor, none of these methods is infallible when applied to a discrete system. This article therefore proposes a new stability criterion, named the Discrete Generalized Bode Criterion (DGBC). This method is based on the Nyquist criterion but developed from the open-loop Bode diagram, evaluated also at 0 Hz and at the Nyquist frequency. The proposed criterion combines the advantages of the Nyquist and Bode criteria, since it is always applicable and provides an interesting and useful tool for the controller design process. The method is applied to design an active damping control of an inverter with LCL filter, showing how the proposed criterion accurately predicts stability, in contrast to the existing Bode criteria. The theoretical analysis is validated through experimental results performed with a three-phase inverter and an LCL filter.

INDEX TERMS Active damping control, control design, frequency domain analysis, LC-filtered voltage source inverter (VSI), stability criteria.

I. INTRODUCTION

The grid connection of renewable energy and Flexible AC Transmission Systems (FACTS) is growing steadily thanks to increasingly competitive costs [1]–[5]. The cost reduction is a result of a number of factors, which often create challenges with regard to the electronic converter control design and stability analysis, such as a reduction in component size [6]–[9], the use of high-power converters to benefit from economies of scale [10], [11], or the use of new topologies [12]–[14]. For this reason, a reliable tool which makes it possible to readily analyze the system stability is of the utmost importance.

Nowadays, the control of the power converter is usually implemented in a microprocessor [15], [16]. As a result, the controller handles digital signals and, strictly speaking, digital control theory should be used for the stability analysis. However, in some situations, the sampling frequency is high enough for the discrete signals to be nearly continuous and, therefore, continuous methods of analysis and design can be employed [17]–[19]. Conversely, other systems show relevant dynamics close to the Nyquist frequency, and the use of continuous modeling methods often results in controls with limited performance and may even lead to incorrect conclusions about stability [20]–[23].

In order to make the most of the electronic converter and microprocessor capability, there are many applications in which the control method dynamically responds at high frequencies near the Nyquist frequency. One example of this situation is the control of the inverters operating within renewable energy plants, where the pressure to optimize the cost has led to a reduction in the size of the output LCL filter. As a result, its resonance frequency increases, moving close to the Nyquist frequency [24]–[28]. At the same time, the control may be required to dynamically respond at the resonance frequency in order to provide active damping. Furthermore, electronic converters must sometimes

The associate editor coordinating the review of this manuscript and approving it for publication was Shafiqul Islam.

control the injected harmonic components, often reaching high frequencies, as in the case of active filters [29]–[31], stand-alone inverters [32], [33], power amplifiers in audio systems [34], or compensation of the PWM voltage distortion [35]–[37]. In the same way, some converters are required to achieve very fast dynamics in order to track the reference or quickly reject the load disturbance, for example in the case of power supplies [38]–[40] and front-end rectifiers [41]. In all these occasions, the system should be modelled as a discrete one and discrete control methods should be applied [17], [20], [24].

Digital control theory appeared subsequent to continuous control theory and adapted the existing stability criteria and design techniques. The original Evans' root locus can be adapted to assess how the closed-loop poles move in the z-plane as one system parameter is modified [16]. However, this method is usually employed to analyze the control robustness rather than to design it since it does not provide any indication about the choice of controller type [24], [25], [42], [43]. Other pole-placement techniques, such as the direct design method of Ragazzini or similar ones, are better suited for the control design since they make it possible to place the closed-loop poles at the desired locations and then determine all controller parameters [17], [44], [45]. The problem here is that high-order controllers are often encountered and it is difficult to select the pole locations which result in feasible controllers [17], [44].

Frequency response methods are currently the most popular for control design in the power electronics sector. The Nyquist stability criterion applied to discrete systems uses information about the open-loop transfer function and is an infallible tool to assess stability [17], [46]–[48]. However, it is still difficult to apply to the controller design process as its plot can be convoluted, making the controller tuning complicated [46]–[49]. In contrast, the Bode stability criterion applied to discrete systems is intuitive and greatly eases the controller design, making it the preferred method within the industry [50], [51], but is based on specific cases of the Nyquist criterion and is only valid under certain conditions [25], [43], [52]. For the purpose of extending the Bode criterion applicability, a number of revisions can be found in the literature [49], [53]–[56]. Among these criteria, the Generalized Bode Criterion (GBC) [56], is the most general and is valid for every continuous feedback loop. However, when adapted to discrete systems, the GBC also fails to determine the stability of certain common systems, as will be shown in this article for an active damping control of an inverter with LCL filter.

This article proposes to extend the generalized Bode criterion to discrete systems. The new method, named Discrete Generalized Bode Criterion (DGBC), is based on the discrete Nyquist criterion but uses the information obtained from the open-loop Bode diagram, evaluated also at 0 Hz and at the Nyquist frequency. Consequently, the proposed criterion combines the advantages of the Nyquist and Bode criteria. It can be applied to any discrete system, as it is based on the discrete Nyquist criterion, and it is also easy to apply to the design of controllers, as it uses information from the Bode diagram.

This article is organized as follows. Section II presents the basis of the DGBC. In section III, as a case-study with dynamics close to the Nyquist frequency, the proposed criterion is applied to design the active damping control of an inverter with LCL filter. It is showed that the DGBC correctly determines its stability, in contrast to the existing Bode criteria. Then, in section IV, experimental results are provided in order to validate the DGBC and, finally, section V concludes this article.

II. PROPOSED STABILITY CRITERION: THE DGBC

A. FORMULATION OF THE DGBC

The block diagram of a sampled-data system is shown in Fig. 1(a), and its discrete equivalent, after determining the z-transform of the continuous plant, is depicted in Fig. 1(b), where $C(z)$ represents the digital controller, $H(z)$ the digital feedback controller, $G(s)$ the continuous plant, $G(z)$ the discretized plant, R denotes the reference signal, U the control signal, Y the output signal, and T_s the sampling time.

To evaluate the stability of the feedback control loop shown in Fig. 1, the discrete Nyquist criterion uses information about the frequency response of the open-loop transfer function, $L(z) = C(z) \cdot G(z) \cdot H(z)$. Provided that the Nyquist diagram is represented for increasing frequencies, from $-\pi < \omega \cdot T_s \leq \pi$, this criterion states that the number of unstable closed-loop poles (outside the unit circle in the z-plane), Z, is equal to the number of unstable open-loop poles, P, minus the total number of anticlockwise encirclements around -1 on the plot, N [17]:

$$Z = P - N. \tag{1}$$

While it is not complicated to obtain P, it can be a complex task to determine N by counting the number of encirclements. A simpler approach to compute N was proposed in [57]. If an auxiliary ray is traced in a random direction starting at -1, then counting the number of times that the ray crosses the Nyquist diagram gives N. As a result, the Nyquist stability criterion can be rewritten as

$$Z = P - N = P - (N_c^+ - N_c^-). \tag{2}$$

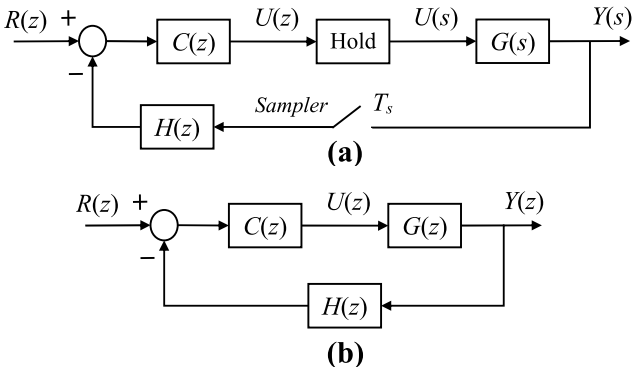

FIGURE 1. Block diagrams: a) sampled-data system, b) discrete equivalent.

where N_c^+ is the number of crossings between the ray and the Nyquist plot with increasing phase, and N_c^- is the number of crossings with decreasing phase.

In [57], it is then proposed to select the ray direction so that the crossings can be obtained using the Bode plot instead of the Nyquist one. In fact, if the ray is placed in the direction of the real negative axis, all crossings have a phase equal to $\pm n \cdot 180°$ (with n an odd number), and a magnitude greater than the unity (greater than 0 dB). These crossings are easy to identify on the Bode diagram, as can be observed in Fig. 2, where C^+ and C^- are the number of crossings counted in the Bode diagram when the phase is increasing and decreasing, respectively.

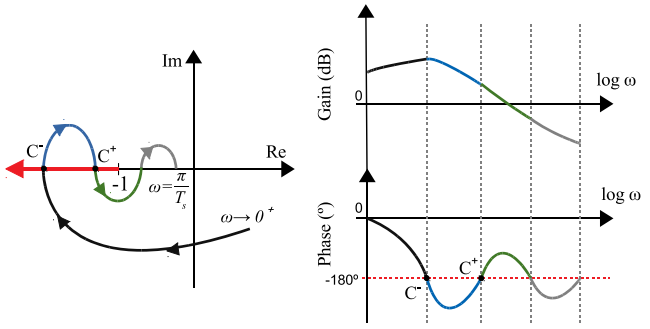

FIGURE 2. Equivalence between Bode and Nyquist diagrams of an open-loop $L(z)$ and their crossings with the ray.

While the Nyquist diagram is defined for positive and negative frequencies, $-\pi < \omega \cdot T_s \leq \pi$, the Bode diagram is only defined for positive frequencies, $0 < \omega \cdot T_s < \pi$. However, given that every $L(z)$ with real coefficients meets

$$L\left(e^{-j\omega T_s}\right) = \overline{L\left(e^{j\omega T_s}\right)}, \tag{3}$$

it can be assured that there is an identical number of crossings at positive and negative frequencies and, as a result, C^+ and C^- must be multiplied by 2 in order to obtain the total number of crossings [56].

Crossings can also appear at 0 Hz. However, since this frequency is not represented in the Bode diagram, the corresponding crossings are not visible, especially when $L(z)$ presents poles at z = 1. At the same time, these poles at z = 1 lead to a complex representation in the Nyquist plot [47]. To avoid this complication, these intersections at 0 Hz can be obtained from a simple table which uses the open-loop transfer function evaluated at 0 Hz, as will be explained in section II.C for discrete systems. The number of these crossings is termed C_0, being positive when occurring with an increasing phase and negative otherwise [56].

Similarly, since the discrete Nyquist diagram is continuous from $\omega = (\pi/T_s)^-$ to $\omega = (-\pi/T_s)^+$ [17], there can also be crossings at the Nyquist frequency, $f_N = f_s/2$ ($\omega_N = \pi/T_s$). Again, as it is difficult to identify these intersections in the Bode plot and they are not visible at all when $L(z)$ has poles at z = −1, they are obtained from the open-loop transfer function evaluated at the Nyquist frequency, as will be explained in section II.B. The number of such crossings is defined as C_N, being positive when occurring with an increasing phase and negative otherwise.

Taking everything into account, the total number of crossings, N, can now be obtained. This leads to the DGBC formulation, which proposes to compute the number of unstable closed-loop poles as

$$Z = P - \left[2 \cdot \left(C^+ - C^-\right) + C_0 + C_N\right]. \tag{4}$$

B. DETERMINATION OF C_N

The value of C_N can be obtained from the open-loop transfer function evaluated at the Nyquist frequency, $f_N = f_s/2$ ($\omega_N = \pi/T_s$). For this purpose, some parameters are first defined. A general form of the open-loop transfer function can be expressed as

$$L(z) = \frac{K_g}{(z-1)^k \cdot (z+1)^l} \cdot \frac{\prod_{i=1}^{N_{Zs}} (z - r_{Zsi})}{\prod_{i=1}^{N_{Ps}} (z - r_{Psi})} \cdot \times \frac{\prod_{i=1}^{N_{Zc}} \left(z^2 - 2r_{Zci}\cos\theta_{Zci} \cdot z + r_{Zci}^2\right)}{\prod_{i=1}^{N_{Pc}} \left(z^2 - 2r_{Pci}\cos\theta_{Pci} \cdot z + r_{Pci}^2\right)} \tag{5}$$

where k is the number of integrators or poles at z = 1, l the number of poles at z = −1 (negative k or l means number of zeros), N_{Ps} the number of other real poles, N_{Pc} the number of pairs of complex conjugate poles, N_{Zs} the number of real zeros, and N_{Zc} the number of pairs of complex conjugate zeros. Parameters r_{Zs} and r_{Ps} can have any value other than 1 or −1, thus including real zeros and poles inside and outside the unit circle. In turn, parameters r_{Zc} and r_{Pc} are always positive and angles θ_{Zc} and θ_{Pc} can have any value from 0 to π, which comprises all possible pairs of complex conjugate poles, inside and outside the unit circle, and also on its circumference.

In order to compute C_N, an important value is the gain of function $L(z)$ without taking into account the poles at z = −1, and evaluated at $\omega = \omega_N$, i.e. for z = −1. This value cannot be obtained by inspection of the Bode plot when $l > 0$, but can be determined analytically, being useful not only for the stability analysis but also for the controller design. This gain, termed K_N, is always a real number (it can be positive or negative), and from (5) can be obtained as

$$K_N = \frac{K_g}{(-2)^k} \cdot \frac{\prod_{i=1}^{N_{Zs}} (-1 - r_{Zsi})}{\prod_{i=1}^{N_{Ps}} (-1 - r_{Psi})} \cdot \times \frac{\prod_{i=1}^{N_{Zc}} \left(1 + 2r_{Zci}\cos\theta_{Zci} + r_{Zci}^2\right)}{\prod_{i=1}^{N_{Pc}} \left(1 + 2r_{Pci}\cos\theta_{Pci} + r_{Pci}^2\right)} \tag{6}$$

When there are poles at $z = -1$, $L(z)$ cannot be evaluated at $\omega = \omega_N = \pi/T_s$, and the original Nyquist contour $z = \exp(j\omega T_s)$ must be modified [17], [58]. In order to exclude these poles, the contour is indented around $z = -1$ as $z = -1 + \varepsilon \cdot \exp(j\phi)$, with ε positive and sufficiently small, and ϕ increasing from $\pi/2$ to $3\pi/2$. Evaluating now $L(z)$ for the indentation leads to

$$L\left(z = -1 + \varepsilon\, e^{j\phi}\right) = \frac{K_N}{\varepsilon^l\, e^{jl\phi}} = \frac{K_N}{\varepsilon^l} e^{-jl\phi}. \tag{7}$$

As can be observed in this expression, as ϕ changes from $\pi/2$ to $3\pi/2$ (ω changes from $(\pi/T_s)^-$ to $(-\pi/T_s)^+$), each pole at $z = -1$ introduces a 180° clockwise rotation in the Nyquist diagram with infinite gain, from $-\pi/2$ to $-3\pi/2$.

Another relevant aspect for the stability assessment is to determine whether the phase of the open-loop in the Nyquist diagram is increasing or decreasing at ω_N. Similarly to parameter K_N, this can be determined analytically by evaluating the sign of the phase derivative at ω_N. Since this derivative does not exist when there are poles at $z = -1$, the lateral derivatives are obtained instead, which are equal due to symmetry, and can be calculated as

$$\begin{aligned}\varphi'_N &= \left.\frac{d\varphi\left(L\left(e^{j\omega T_s}\right)\right)}{d\omega}\right|_{\omega=(\frac{\pi}{T})^-} = \left.\frac{d\varphi\left(L\left(e^{j\omega T_s}\right)\right)}{d\omega}\right|_{\omega=(-\frac{\pi}{T})^+} = \\ &= \sum_{i=1}^{N_{Zs}} \frac{T_s}{1 + r_{Zsi}} + \sum_{i=1}^{N_{Zc}} \frac{2T_s \cdot (1 + r_{Zci}\cos\theta_{Zci})}{1 + 2r_{Zci}\cos\theta_{Zci} + r_{Zci}^2} \\ &\quad - \frac{T_s}{2} \cdot (k + l) - \sum_{i=1}^{N_{Ps}} \frac{T_s}{1 + r_{Psi}} \\ &\quad - \sum_{i=1}^{N_{Pc}} \frac{2T_s \cdot (1 + r_{Pci}\cos\theta_{Pci})}{1 + 2r_{Pci}\cos\theta_{Pci} + r_{Pci}^2}.\end{aligned} \tag{8}$$

Now that K_N and φ'_N are identified, the value of C_N is analyzed for different numbers of poles at $z = -1$ up to 2 ($l \leq 2$). The cases with more poles at $z = -1$ could be analyzed following the same reasoning. The corresponding Nyquist diagrams are shown in Fig. 3, where the values at frequencies $\omega = (-\pi/T_s)^+, 0^-, 0^+$ and $(\pi/T_s)^-$ are highlighted. The values of C_N for the cases studied are summarized in Table 1.

1) $L(z)$ With Zeros $z = -1$ ($l < 0$): In this case, the Nyquist plot at ω_N is located at the origin and thus C_N is always 0.

2) $L(z)$ With No Poles at $z = -1$ ($l = 0$): The Nyquist diagram at ω_N is placed at K_N, always in the real axis (see Fig. 3(a)-(c)). When $K_N > -1$, the value at ω_N is situated to the right of -1 (see Fig. 3(a)). Consequently, no crossings occur with the auxiliary ray, which is highlighted in red in the figure, leading to $C_N = 0$. However, if $K_N < -1$, the diagram at ω_N is placed just on the ray (see Fig. 3(b) and (c)). In this situation, if $\varphi'_N > 0$, the phase is increasing and thus $C_N = +1$. Conversely, if $\varphi'_N < 0$, the phase is decreasing and then $C_N = -1$.

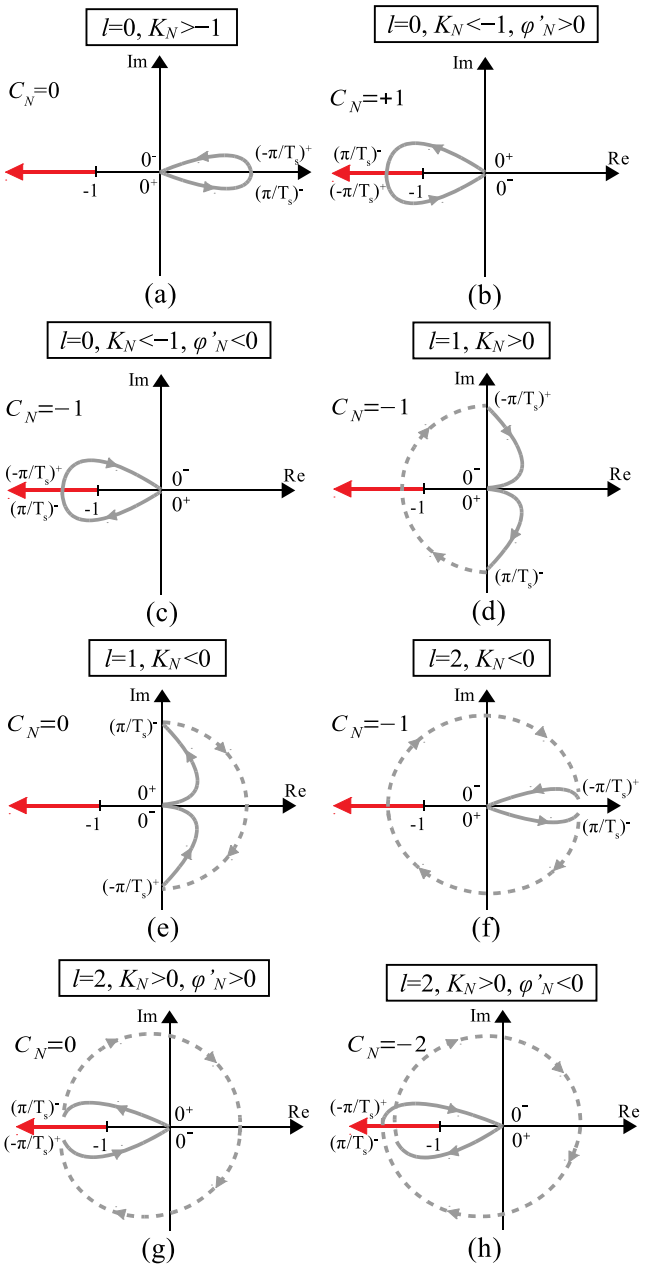

FIGURE 3. Nyquist diagrams and value of C_N for different transfer functions.

3) $L(z)$ With One Pole at $z = -1$ ($l = 1$): As shown in (7), the presence of the pole at $z = -1$ produces, around ω_N, a 180° clockwise rotation in the Nyquist diagram with infinite gain, which is represented by dashed lines in Fig. 3. When considering only this pole, the phase goes from $-90°$ at $\omega = (\pi/T_s)^-$ to $-270°$ at $\omega = (-\pi/T_s)^+$. As a result, if $K_N > 0$, there is one crossing with the auxiliary ray at ω_N, leading to $C_N = -1$ (see Fig. 3(d)). On the other hand, if $K_N < 0$, the phase goes from $+90°$ at $\omega = (\pi/T_s)^-$ to $-90°$ at $\omega = (-\pi/T_s)^+$, no crossings occur, and $C_N = 0$ (see Fig. 3(e)).

4) $L(z)$ With Two Poles at $z = -1$ ($l = 2$): The two poles at $z = -1$ provoke a 360° clockwise rotation in the Nyquist

TABLE 1. Determination of C_N for open-loop transfer functions with up to two poles at z = −1.

Number of poles at z = −1 (l)	Gain without poles at z = −1 (K_N)	Phase derivative at ω_N (φ'_N)	Crossings at ω_N (C_N)
$l < 0$	-	-	0
$l = 0$	$K_N > -1$	-	0
	$K_N < -1$	$\varphi'_N > 0$	+1
		$\varphi'_N < 0$	−1
$l = 1$	$K_N > 0$	-	−1
	$K_N < 0$	-	0
$l = 2$	$K_N > 0$	$\varphi'_N > 0$	0
		$\varphi'_N < 0$	−2
	$K_N < 0$	-	−1

diagram with infinite gain at ω_N, from $-180°$ at $\omega = (\pi/T_s)^-$ to $-540°$ at $\omega = (-\pi/T_s)^+$. Therefore, if $K_N < 0$, the phase goes from $0°$ at $\omega = (\pi/T_s)^-$ to $-360°$ at $\omega = (-\pi/T_s)^+$, and one crossing always occurs, leading to $C_N = -1$ (see Fig. 3(f)). If $K_N > 0$, the Nyquist diagram is placed on the ray for both $\omega = (\pi/T_s)^-$ and $\omega = (-\pi/T_s)^+$. Under these circumstances, increasing phase at ω_N, $\varphi'_N > 0$, means that $\varphi((\pi/T_s)^-) < -180°$ and $\varphi((-\pi/T_s)^+) > -540°$, resulting in no crossings and $C_N = 0$ (see Fig. 3(g)). On the contrary, decreasing phase $\varphi'_N < 0$ results in $\varphi((\pi/T_s)^-) > -180°$ and $\varphi((-\pi/T_s)^+) < -540°$, which leads to two crossings, $C_N = -2$ (see Fig. 3(h)).

C. DETERMINATION OF C_0

The value of C_0 can be obtained in a similar way to C_N by analyzing the open-loop transfer function at $\omega = 0$. For this reason, the procedure is summarized below.

The gain of function $L(z)$ without integrators evaluated at $\omega = 0$, i.e. for z = 1, is defined as K_0. This gain is always a real number (it can be positive or negative), and from (5) can be obtained as

$$K_0 = \frac{K_g}{2^l} \cdot \frac{\prod_{i=1}^{N_{Zs}} (1 - r_{Zsi})}{\prod_{i=1}^{N_{Ps}} (1 - r_{Psi})} \cdot \frac{\prod_{i=1}^{N_{Zc}} \left(1 - 2r_{Zci}\cos\theta_{Zci} + r_{Zci}^2\right)}{\prod_{i=1}^{N_{Pc}} \left(1 - 2r_{Pci}\cos\theta_{Pci} + r_{Pci}^2\right)}. \tag{9}$$

It is also important to know whether the phase of the open-loop in the Nyquist diagram is increasing or decreasing at $\omega = 0$, which can be determined analytically by evaluating the sign of the phase derivative at 0. Since this derivative does not exist when there are integrators, the lateral derivatives are calculated instead, which are equal due to symmetry, and can be calculated as

$$\varphi'_0 = \left.\frac{d\varphi\left(L\left(e^{j\omega T_s}\right)\right)}{d\omega}\right|_{\omega=0^+} = \left.\frac{d\varphi\left(L\left(e^{j\omega T_s}\right)\right)}{d\omega}\right|_{\omega=0^-} =$$
$$= \sum_{i=1}^{N_{Zs}} \frac{T_s}{1 - r_{Zsi}} + \sum_{i=1}^{N_{Zc}} \frac{2T_s \cdot (1 - r_{Zci}\cos\theta_{Zci})}{1 - 2r_{Zci}\cos\theta_{Zci} + r_{Zci}^2}$$

TABLE 2. Determination of C_0 for open-loop transfer functions with up to two integrators.

Number of integrators (k)	DC gain without integrators (K_0)	Phase derivative at 0 Hz (φ'_0)	Crossings at 0 Hz (C_0)
$k < 0$	-	-	0
$k = 0$	$K_0 > -1$	-	0
	$K_0 < -1$	$\varphi'_0 > 0$	+1
		$\varphi'_0 < 0$	−1
$k = 1$	$K_0 > 0$	-	0
	$K_0 < 0$	-	−1
$k = 2$	$K_0 > 0$	$\varphi'_0 > 0$	0
		$\varphi'_0 < 0$	−2
	$K_0 < 0$	-	−1

$$- \frac{T_s}{2} \cdot (k + l) - \sum_{i=1}^{N_{Ps}} \frac{T_s}{1 - r_{Psi}} - \sum_{i=1}^{N_{Pc}} \frac{2T_s \cdot (1 - r_{Pci}\cos\theta_{Pci})}{1 - 2r_{Pci}\cos\theta_{Pci} + r_{Pci}^2}. \tag{10}$$

In contrast to continuous systems, this expression shows that the integrators do contribute to the phase derivative in discrete systems.

Knowing the parameters K_0 and φ'_0, the value of C_0 can be obtained depending on the number of integrators and is given in Table 2 up to two ($k \leq 2$). The cases with more integrators are not of practical interest. For more information about how this table is prepared, the reader can refer to [56], where the value of C_0 is analyzed for continuous systems in a similar way to how the value of C_N is computed for discrete systems in section II.B. When observing Table 1 and 2 for the calculation of C_N and C_0, respectively, it can be seen that all values are equal except for case $l = 1$ and $k = 1$. This can be explained by comparing the effect at ω_N of one pole at z = −1 with the influence at $\omega = 0$ of one integrator. Whereas the former modifies the phase from $-90°$ at $\omega = (\pi/T_s)^-$ to $-270°$ at $\omega = (-\pi/T_s)^+$, the latter modifies it from $+90°$ at 0^- to $-90°$ at 0^+, giving rise to a difference of $-180°$ between them. For this reason, rows with even l and k will be equivalent in relation to C_N and C_0 while rows with odd l and k will differ in the sign of K_N and K_0.

D. DETERMINATION OF C_N AND C_0 BY INSPECTION

In the previous sections, the values of C_N and C_0 are obtained from Table 1 and Table 2, respectively. For this purpose, the detailed system model is required. However, in some occasions the designer has no information about the transfer function expression but instead obtains the Bode plot by frequency response measurements. In this case, it is also possible to determine C_N and C_0 by inspection of the Bode diagram.

TABLE 3. Determination of C_N by inspection for open-loop transfer functions with up to two poles at z = −1.

Gain at $\omega=\omega_N$ (dB_N)	Phase at $\omega\to\omega^-_N$ (φ^-_N)	Phase derivative at $\omega\to\omega^-_N$ (φ'_N)	Crossings at ω_N (C_N)
$dB_N<0$	-	-	0
$dB_N>0$ (finite)	$\varphi^-_N\approx 0$	-	0
	$\varphi^-_N\approx -180^o$	$\varphi'_N>0$ ($\varphi^-_N<-180^o$)	+1
		$\varphi'_N<0$ ($\varphi^-_N>-180^o$)	−1
$dB_N\to\infty$	$\varphi^-_N\approx 0$	-	−1
	$\varphi^-_N\approx -90^o$	-	−1
	$\varphi^-_N\approx -180^o$	$\varphi'_N>0$ ($\varphi^-_N<-180^o$)	0
		$\varphi'_N<0$ ($\varphi^-_N>-180^o$)	−2
	$\varphi^-_N\approx -270^o$	-	0

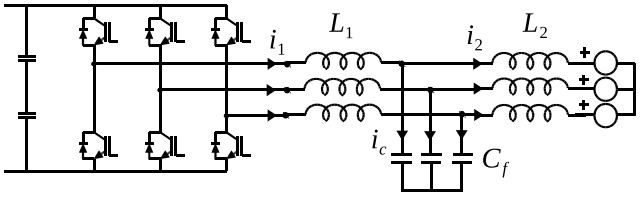

FIGURE 4. Three-phase grid-connected converter with LCL filter.

Table 3 shows how to obtain the value of C_N by the inspection of the Bode diagram near the Nyquist frequency ω_N, for open-loop transfer function with up to two poles at z = −1. With this aim, one must first evaluate the magnitude at $\omega=\omega_N$, dB_N, and the phase at $\omega\to\omega_N^-$, φ_N^-, which are easily obtained from the Bode plot.

1) dB_N < 0: In this case, it is not important if there are crossings with $\pm n\cdot 180°$ (with n an odd number), since they would not be counted, always resulting in $C_N=0$.

2) dB_N> 0 and Finite: A finite dB_N value means that there are no poles at z = −1. Thus, the phase can only be $\varphi_N^-\approx 0$, i.e. there are no crossings and $C_N=0$, or $\varphi_N^-\approx -180°$, i.e. there is one crossing. The sign of this crossing can be determined by analyzing the phase variation in the Bode plot, at frequencies just below the Nyquist frequency. If the phase is increasing ($\varphi'_N>0$), or equivalently the phase is lower than $-180°$ ($\varphi_N^-<-180°$), then $C_N=+1$ (see Fig. 3(b)). In contrast, if the phase is decreasing ($\varphi'_N<0$), or equivalently the phase is higher than $-180°$ ($\varphi_N^->-180°$), $C_N=-1$ (see Fig. 3(c)).

3) $dB_N\to\infty$: An infinite dB_N value means that there are one or two poles at z = −1. In the case with one pole, the phase can be $\varphi_N^-\approx -90°$, which leads to $C_N=-1$ (see Fig. 3(d)), or $\varphi_N^-\approx -270°$, resulting in $C_N=0$ (see Fig. 3(e)). On the other hand, with two poles at z = −1, the phase can be $\varphi_N^-\approx 0$, leading to $C_N=-1$ (see Fig. 3(f)) or $\varphi_N^-\approx -180°$. In the latter case, the number of crossings again depends on the phase variation at frequencies just below the Nyquist frequency. If the phase is increasing ($\varphi'_N>0$), or equivalently the phase is lower than $-180°$ ($\varphi_N^-<-180°$), then $C_N=0$ (see Fig. 3(g)). In contrast, if the phase is decreasing ($\varphi'_N<0$), or equivalently the phase is higher than $-180°$ ($\varphi_N^->-180°$), $C_N=-2$ (see Fig. 3(h)).

TABLE 4. Determination of C_0 by inspection for open-loop transfer functions with up to two integrators.

Gain at $\omega\to 0^+$ (dB_0)	Phase at $\omega\to 0^+$ (φ^+_0)	Phase derivative at $\omega\to 0^+$ (φ'_0)	Crossings at 0 (C_0)
$dB_0<0$	-	-	0
$dB_0>0$ (finite)	$\varphi^+_0\approx 0$	-	0
	$\varphi^+_0\approx -180^o$	$\varphi'_0>0$ ($\varphi^+_0>-180^o$)	+1
		$\varphi'_0<0$ ($\varphi^+_0<-180^o$)	−1
$dB_0\to\infty$	$\varphi^+_0\approx 0$	-	−1
	$\varphi^+_0\approx -90^o$	-	0
	$\varphi^+_0\approx -180^o$	$\varphi'_0>0$ ($\varphi^+_0>-180^o$)	0
		$\varphi'_0<0$ ($\varphi^+_0<-180^o$)	−2
	$\varphi^+_0\approx -270^o$	-	−1

Following a similar reasoning, the value of C_0 can be obtained by the inspection of the Bode diagram near 0 Hz, for open-loop transfer function with up to two integrators, and is shown in Table 4. For this purpose, one must first evaluate the magnitude at $\omega\to 0^+$, dB_0, and the phase at $\omega\to 0^+$, φ_0^+, which are easily obtained from the Bode plot.

III. CASE-STUDY: DESIGN OF AN ACTIVE DAMPING CONTROL OF AN INVERTER WITH LCL FILTER

A. OPEN-LOOP WITH NO POLES AT Z = −1: ACTIVE DAMPING WITH CAPACITOR CURRENT FEEDBACK

Figure 4 shows a three-phase voltage-source converter connected to the grid through an LCL filter. The filter comprises a converter-side inductor L_1, a capacitor C_f, and a grid-side inductor L_2, which includes the filter and the equivalent grid inductances. The equivalent series resistances are small and can be disregarded for the analysis.

This converter controls the current injected into the grid. Converter-side current can be controlled in $\alpha\beta$ axis as represented in Fig. 5. This diagram includes the active damping of the LCL filter by using the capacitor current feedback, which is the focus of the case study. In the figure, $C(z)$ represents the current controller, $H(z)$ the feedback controller, z^{-1} the computational delay, ZOH the zero-order hold, $G_{ic}(s)$ the control to capacitor current transfer function, $G_{i1ic}(s)$ the transfer function which relates i_c and i_1, $H_i(s)$ the anti-aliasing current filter, and T_s the sampling time.

The plant for the active damping, $G_{ic}(s)$, and its corresponding z-domain transfer function after applying the ZOH discretization, $G_{ic}(z)$, can be expressed as [15]

$$G_{ic}(s)=\frac{i_c(s)}{v(s)}=\frac{1}{L_1}\cdot\frac{s}{s^2+\omega_r^2}, \tag{11}$$

$$G_{ic}(z)=\frac{i_c(z)}{v(z)}=\frac{\sin(\omega_r T_s)}{\omega_r L_1}\cdot\frac{z-1}{z^2-2z\cos(\omega_r T_s)+1}, \tag{12}$$

where ω_r is the filter resonance frequency, defined as

$$\omega_r=\sqrt{\frac{L_1+L_2}{L_1 L_2 C_f}}. \tag{13}$$

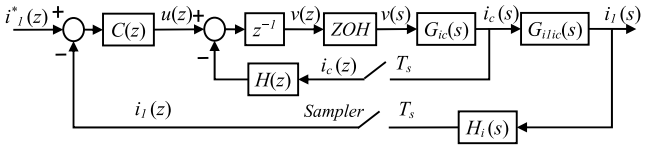

FIGURE 5. Block diagram of the current control with active damping based on the capacitor current.

As can be observed in (11) and (12), the system plant has two resonant poles at ω_r, which complicates the design of the current control and reduces its bandwidth. To avoid these problems, capacitor current feedback is included in order to increase the damping of these poles. The proposed DGBC will be used to design the active damping control. For this purpose, the open-loop transfer function is required and can be obtained as

$$L(z) = H(z) \cdot z^{-1} \cdot G_{ic}(z). \tag{14}$$

Most frequently, a constant feedback controller is selected, $H(z) = K_d$, where K_d is the damping constant and can be positive or negative [22], [59]. Thus, from (12) and (14), the open-transfer function becomes

$$L(z) = K_d \cdot \frac{\sin(\omega_r T_s)}{\omega_r L_1} \cdot \frac{z-1}{z} \cdot \frac{1}{z^2 - 2z\cos(\omega_r T_s) + 1}. \tag{15}$$

As can be observed, $L(z)$ includes one pole with $r = 0$ due to the computational delay, one zero at z = 1, and two resonant poles with $r = 1$ and $\theta = \omega_r \cdot T_s$.

In order to carry out the stability analysis and controller design with the DGBC, the number of closed-loop unstable poles is evaluated by means of (4). For this purpose, the value of P, C^+, C^-, C_0 and C_N must be computed. There are no open-loop unstable poles in (15) and thus $P = 0$. In addition, the zero at z = 1 translates to $k = -1$ and, from Table 2, C_0 is always 0. Therefore, in this case both P and C_0 are independent of the parameters and are not relevant for the design. Examples in which they are important in the controller design can be consulted in [56] and [60].

Then, from (15), the phase of $L(z)$ can be calculated as

$$\varphi\left(L\left(e^{j\omega T_s}\right)\right) = \pi/2 \cdot sign(K_d) - 3/2 \cdot \omega \cdot T_s, \quad if\ \omega < \omega_r$$
$$\varphi\left(L\left(e^{j\omega T_s}\right)\right) = \pi/2 \cdot sign(K_d) - \pi - 3/2 \cdot \omega \cdot T_s, \quad if\ \omega > \omega_r \tag{16}$$

where the delay of $-3/2{\cdot}\omega \cdot T_s$ is due to the computational delay together with the ZOH, and the abrupt phase reduction of π at ω_r is due to the resonance.

Equation (16) shows that the open-loop phase decreases for all frequencies. Thus, in this situation, C^+ is always 0 and C_N can only be 0 or negative. Taking everything into account, from the DGBC equation, (4), the number of closed-loop unstable poles, Z, is

$$Z = 2 \cdot C^- - C_N = 2 \cdot C^- + |C_N|. \tag{17}$$

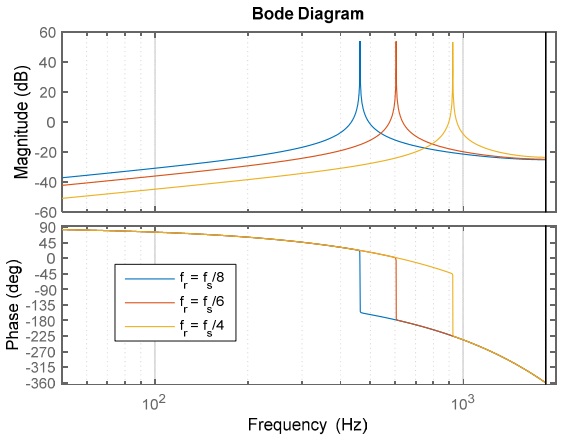

FIGURE 6. Bode diagram of the open-loop transfer function for positive proportional feedback of the capacitor current.

Thus, $C^- = 0$ and $C_N = 0$ are necessary conditions to avoid unstable poles for active damping with proportional capacitor current feedback.

For $K_d > 0$, the Bode plot of the open-loop transfer function, $L(z)$, is represented in Fig. 6 for three different ratios between the resonance and the sampling frequencies. The effect of the resonant poles and the phase tendency as stated by (16) can be clearly observed. To obtain the number of crossings at ω_N, C_N is computed using Table 1. There are no poles at z = −1, so $l = 0$. In addition, $K_d > 0$ leads to $K_N = L(z = -1) > 0$ from (15). Thus, by using the table, C_N is equal to 0. Concerning C^-, Fig. 6 shows that there is always one crossing with −180°, which must be counted if the gain is higher than 0 dB. From the yellow curve in the figure or (16), it is clear that the crossing occurs at ω_r when $f_r > f_s/6$. This crossing is with infinite gain, leading to $C^- = 1$ and two unstable poles, $Z = 2$. In contrast, when $f_r < f_s/6$, it can be obtained from (16) that the crossing is at $f = f_s/6$, which is after the resonance in this case (see the blue curve in Fig. 6). At this frequency, $\omega \cdot T_s = \pi/3$ and, from (15), the open-loop magnitude is

$$\left|L(e^{j\pi/3})\right| = \frac{K_d}{\omega_r L_1} \cdot \frac{\sin(\omega_r T_s)}{2\cos(\omega_r T_s) - 1}. \tag{18}$$

In order to have $C^- = 0$, this gain must be lower than 1 and the maximum value of the proportional gain, $K_{d,max}$, is obtained in (19). Thus, $K_d > K_{d,max}$ leads to $C^- = 1$ and two unstable poles appear in the closed-loop. However, with $K_d < K_{d,max}$, then $C^- = 0$ and the active damping loop is stable, although its effect is very weak when f_r is close to $f_s/6$.

$$K_{d,\max} = \omega_r L_1 \cdot \frac{2\cos(\omega_r T_s) - 1}{\sin(\omega_r T_s)}. \tag{19}$$

The conclusions about the stability analysis with proportional and positive feedback of the capacitor current are summarized in the first half of Table 5. As can be observed, active damping can be provided only when f_r is below $f_s/6$.

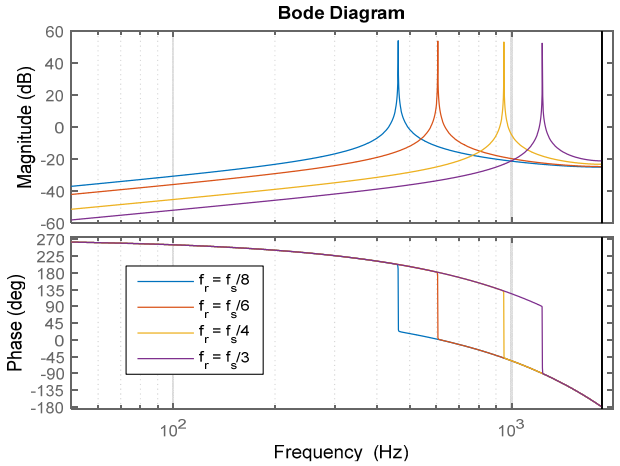

FIGURE 7. Bode diagram of the open-loop transfer function for negative proportional feedback of the capacitor current.

However, in high-power converters f_r is usually higher than $f_s/6$ and this method will become unstable. In this case, it is better to use a negative gain K_d as proportional feedback. As stated above, for $K_d < 0$, (15)–(17) apply and $P = C_0 = C^+ = 0$, meaning that $C^- = 0$ and $C_N = 0$ are again necessary conditions for stability.

For $K_d < 0$, the Bode plot of the open-loop transfer function, $L(z)$, is represented in Fig. 7 for four different ratios between the resonance and the sampling frequencies. It can be observed that there is always one crossing with $+180°$ and decreasing phase, which must be counted if the gain is higher than 1 (higher than 0 dB). From the blue curve or (16), this crossing is at ω_r when $f_r < f_s/6$, resulting in $C^- = 1$ and an unstable control. However, when $f_r > f_s/6$, it can be obtained from (16) that the crossing is at $f = f_s/6$, which is below the resonance (see the yellow and purple curves in Fig. 7). At this frequency, $\omega \cdot T_s = \pi/3$ and, from (15), the open-loop gain, and the maximum value of the proportional gain to achieve $C^- = 0$, can be obtained as

$$\left|L(e^{j\pi/3})\right| = \frac{|K_d|}{\omega_r L_1} \cdot \frac{\sin(\omega_r T_s)}{1 - 2\cos(\omega_r T_s)}, \tag{20}$$

$$\left|K_{d,\max,C-}\right| = \omega_r L_1 \cdot \frac{1 - 2\cos(\omega_r T_s)}{\sin(\omega_r T_s)}. \tag{21}$$

In order to determine C_N, the crossings at ω_N must be evaluated. In this case, since $l = 0$ and $K_N < 0$, there is always one crossing with -180 at ω_N, as can be observed in Fig. 7. From Table 1, to accomplish $C_N = 0$, K_N must be higher than -1, in other words,

$$K_N = \frac{K_d}{\omega_r L_1} \cdot \frac{\sin(\omega_r T_s)}{1 + \cos(\omega_r T_s)} = \frac{K_d}{\omega_r L_1} \cdot \tan\left(\frac{\omega_r T_s}{2}\right) > -1 \tag{22}$$

From this equation, the maximum value of the proportional gain which ensures $C_N = 0$ can be derived as

$$\left|K_{d,\max,Cn}\right| = \omega_r L_1 \cdot \frac{1}{\tan(\omega_r T_s/2)}. \tag{23}$$

TABLE 5. Stability analysis for active damping with proportional feedback of the capacitor current.

Case	$f_r < f_s/6$	$f_s/6 < f_r < f_s/4$	$f_s/4 < f_r$
$K_d > 0$ $K_{d,max}$ (19)	$K_d < K_{d,max}$ **Z = 0**	$C^- = 1 \rightarrow$ **Z = 2**	$C^- = 1 \rightarrow$ **Z = 2**
	$K_d > K_{d,max}$ $C^- = 1$, **Z = 2**		
$K_d < 0$ $\lvert K_{d,max,C-}\rvert$(21) $\lvert K_{d,max,Cn}\rvert$(23)	$\lvert K_d\rvert < \lvert K_{d,max,Cn}\rvert$ $C^- = 1$, $C_N = 0$ **Z = 2**	$\lvert K_d\rvert < \lvert K_{d,max,C-}\rvert$ $C^- = 0$, $C_N = 0$ **Z = 0**	$\lvert K_d\rvert < \lvert K_{d,max,Cn}\rvert$ $C^- = 0$, $C_N = 0$ **Z = 0**
		$\lvert K_d\rvert > \lvert K_{d,max,C-}\rvert$ $\lvert K_d\rvert < \lvert K_{d,max,Cn}\rvert$ $C^- = 1$, $C_N = 0$ **Z = 2**	$\lvert K_d\rvert > \lvert K_{d,max,Cn}\rvert$ $\lvert K_d\rvert < \lvert K_{d,max,C-}\rvert$ $C^- = 0$, $C_N = -1$ **Z = 1**
	$\lvert K_d\rvert > \lvert K_{d,max,Cn}\rvert$ $C^- = 1$, $C_N = -1$ **Z = 3**	$\lvert K_d\rvert > \lvert K_{d,max,C-}\rvert$ $\lvert K_d\rvert > \lvert K_{d,max,Cn}\rvert$ $C^- = 1$, $C_N = -1$ **Z = 3**	$\lvert K_d\rvert > \lvert K_{d,max,Cn}\rvert$ $\lvert K_d\rvert > \lvert K_{d,max,C-}\rvert$ $C^- = 1$, $C_N = -1$ **Z = 3**

The conclusions about the stability analysis with proportional and negative feedback of the capacitor current are summarized in Table 5. As can be observed, the proportional and negative feedback of the capacitor current is able to provide active damping when f_r is above $f_s/6$, given that the conditions (21) and (23) are fulfilled. It can be verified that the constraint (21) is more restrictive when $f_r < f_s/4$, while the constraint (23) becomes more restrictive when $f_r > f_s/4$.

Using the GBC instead of the proposed DGBC can result in important errors about stability. Specifically, applying the GBC for a system with $f_r < f_s/4$ will lead to $C^- = 0$ as necessary condition for stability. As a consequence, when (21) is fulfilled but (23) is not, the GBC will predict stability while it has been shown that one unstable pole will appear. This case is represented in intense red in Table 5.

B. ADVANTAGES OF THE DESIGN WITH DGBC: ACTIVE DAMPING WITH VARIABLE RESONANT FREQUENCY

In order to design an active damping control of a grid-connected inverter with LCL filter, the variation range of the grid inductance must be taken into account, which leads to the appearance of a variable resonant frequency. As an example, in this section the DGBC will be used for the design of an active damping method with capacitor current feedback, as shown in Fig. 5, for a system in which the grid short-circuit ratio can vary from 20 to 6, which translates to a resonant frequency variation range from $f_r = f_s/6.5$ to $f_r = f_s/5$.

When using a constant feedback controller H(z) = K_d, the analysis made in section III.A by means of the DGBC (see Table 5) shows that it is not possible to remain stable for the whole resonant frequency range. This analysis can also be carried out using the Nyquist diagram of the open-loop transfer function, (see (15)), which is represented in Fig. 8 for $K_d > 0$ and the boundary frequencies $f_r = f_s/6.5$ and

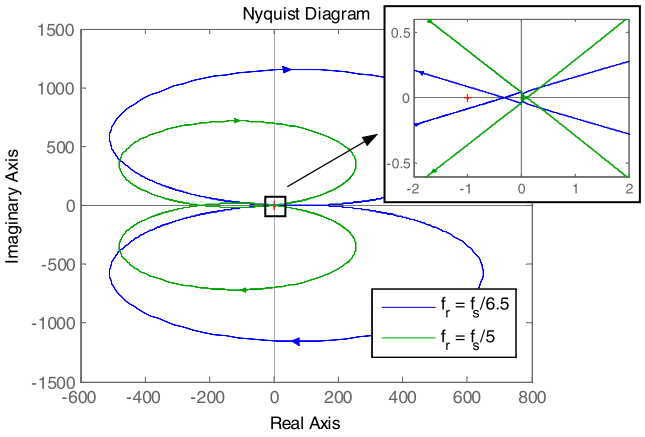

FIGURE 8. Nyquist diagram of the open-loop transfer function for positive proportional feedback of the capacitor current.

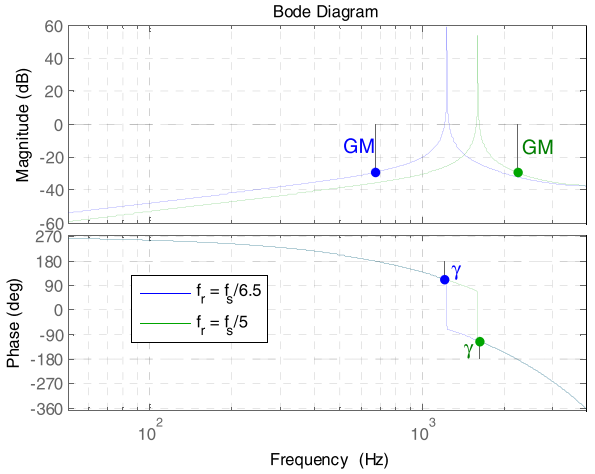

FIGURE 9. Bode diagram of the open-loop transfer function for the feedback controller (24) and using the capacitor current.

$f_r = f_s/5$. Since there are no open-loop poles, and the number of anticlockwise encirclements around -1 is $N = 0$ for $f_r = f_s/6.5$ and $N = -2$ for $f_r = f_s/5$, the Nyquist stability criterion confirms that the damping method will be stable for $f_r = f_s/6.5$ and unstable for $f_r = f_s/5$. Comparing this figure with the Bode diagram shown in Fig. 6, it can be observed that it is much more complicated to count the encirclements around -1 in the Nyquist diagram than the $-180°$ crossings with positive magnitude in the Bode plot. For other systems which include integrators and more resonant poles, for example due the presence of multi-resonant controllers, the advantage of the Bode criterions become even clearer (see Fig. 8 in [56]).

In any case, the most important advantage of the Bode criterions arises from the controller design, which explains its success within the industry [50], [51]. Focusing on the Nyquist diagram shown in Fig. 8, it is difficult for the designer to know how the controller H(z) should be modified in order to make the control stable for both cases. However, looking at the Bode diagram for $K_d > 0$, shown in Fig. 6, it is clear to see that the open-loop phase could be increased in order to avoid the $-180°$ crossing with positive magnitude. Similarly, focusing on the Bode diagram for $K_d < 0$, shown in Fig. 7, in this case it is intuitive to realize that the open-loop phase could be decreased in order to avoid the 180° crossing with positive magnitude.

Although both alternatives are suitable to make the damping method stable for the whole resonant frequency range, the design of the latter solution is chosen for demonstration since it is superior in terms of noise rejection. For this purpose, a feedback controller which includes a real pole is selected. Its expression and its phase can be written as

$$H(z) = K_d \cdot \frac{1-r}{z-r}, \quad K_d < 0, \tag{24}$$

$$\varphi\left(H(e^{j\omega T_s})\right) = -\frac{\omega \cdot T_s}{2} - \arctan\left(\frac{1+r}{1-r} \cdot \tan\left(\frac{\omega \cdot T_s}{2}\right)\right), \tag{25}$$

where r represents the location of the pole.

In order to apply the DGBC, the Bode diagram of the compensated open-loop transfer function is represented in Fig. 9 for $f_r = f_s/6.5$ and $f_r = f_s/5$. The location of the controller pole $z = r$ is chosen so that the minimum phase distance to $+180°$ or $-180°$ at the resonant frequency, named γ, is equal for both curves. There are no open-loop unstable poles so $P = 0$. From the figure or the corresponding tables, there are no crossings at 0 Hz or at the Nyquist frequency, which results in $C_0 = C_N = 0$. Furthermore, since there are no crossings with increasing phase, one also obtains $C^+ = 0$. Finally, for each curve, there are two crossings with decreasing phase, which must be counted if the gain is higher than 0 dB. The minimum gain margin GM is represented for each curve, which in this case is the same due to symmetry. Since the diagram is plotted for $K_d = -1$, the gain margin provides the maximum value of the damping constant to achieve $C^- = 0$ and thus a stable control, in this example $|K_{d,max}| = 29.2$.

C. OPEN-LOOP WITH ONE POLE AT Z = −1: ACTIVE DAMPING WITH CAPACITOR VOLTAGE FEEDBACK

As shown in section III.A, active damping based on negative proportional feedback of the capacitor current is effective for $f_r > f_s/6$. However, as f_r approaches $f_s/2$, the maximum feedback constant is limited to very low values as dictated by (23), and thus the active damping effect becomes very weak. As a result, in applications where f_r is around or above $f_s/2$ [25]–[27], an interesting alternative is to use the proportional feedback of the capacitor voltage. The corresponding diagram is shown in Fig. 10, where $G_{vc}(s)$ is the control to capacitor voltage transfer function, and $G_{i1vc}(s)$ the transfer function which relates v_c and i_1.

The plant for the active damping, $G_{vc}(s)$, and its corresponding z-domain transfer function after applying the ZOH discretization, $G_{vc}(z)$, can be expressed as [15]

$$G_{vc}(s) = \frac{v_c(s)}{v(s)} = \frac{1}{L_1 C_f} \cdot \frac{1}{s^2 + \omega_r^2}, \tag{26}$$

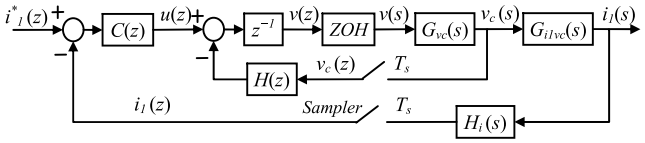

FIGURE 10. Block diagram of the current control with active damping based on the capacitor voltage.

$$G_{vc}(z) = \frac{v_c(z)}{v(z)} = \frac{L_2}{L_1 + L_2}\left(1 - \cos\left(\omega_r T_s\right)\right) \cdot \times \frac{z+1}{z^2 - 2z\cos\left(\omega_r T_s\right) + 1}. \quad (27)$$

Although the DGBC can be applied to any discrete system, the purpose of this subsection is to show how to apply the method to a real system in which there are poles at z $= -1$. For this reason, it is considered that the resonance frequency is equal to the Nyquist frequency, i.e. $f_r = f_s/2$. Although this equality may not be imposed by design, it is very likely to occur due to grid inductance variations when the rated values of f_r and $f_s/2$ are not far from each other [25], [26]. In this situation, $\omega_r \cdot T_s = \pi$ and, from (27), the plant becomes

$$G_{vc}(z) = \frac{v_c(z)}{v(z)} = \frac{2L_2}{L_1 + L_2} \cdot \frac{1}{z+1}. \quad (28)$$

Including now the computational delay and a constant feedback controller, $H(z) = K_v$, where K_v is the damping constant, the open-loop transfer function can be obtained as

$$L(z) = K_v \cdot \frac{2L_2}{L_1 + L_2} \cdot \frac{1}{z} \cdot \frac{1}{z+1}. \quad (29)$$

As can be observed, $L(z)$ includes one pole with $r = 0$ due to the computational delay, and one pole at z $= -1$ due to the concurrence of the resonance and Nyquist frequencies.

To perform the stability analysis and controller design, the DGBC is now applied to the open-loop transfer function. For this purpose, the value of P, C^+, C^-, C_0 and C_N in (4) must be computed. There are no open-loop unstable poles in (29), so $P = 0$.

From (27), the phase of $L(z)$ can be determined as

$$\varphi\left(L\left(e^{j\omega T_s}\right)\right) = \frac{1 - sign\left(K_v\right)}{2} \cdot \pi - {}^3\!/_2 \cdot \omega \cdot T_s, \quad if\ \omega < \omega_N. \quad (30)$$

This equation shows that the open-loop phase decreases for all frequencies below ω_N. Thus, C^+ is always 0 whereas C_0 can only be 0 or negative. Furthermore, since there is one pole at z $= -1$, $l = 1$ and, from Table 1, C_N can only be 0 or negative. Taking everything into account, from the DGBC equation, (4), the number of closed-loop unstable poles, Z, is

$$Z = 2 \cdot C^- - C_0 - C_N = 2 \cdot C^- + |C_0| + |C_N|. \quad (31)$$

Thus, $C^- = 0$, $C_0 = 0$ and $C_N = 0$ are necessary conditions to avoid unstable poles for active damping with proportional feedback of capacitor voltage when $f_r = f_s/2$.

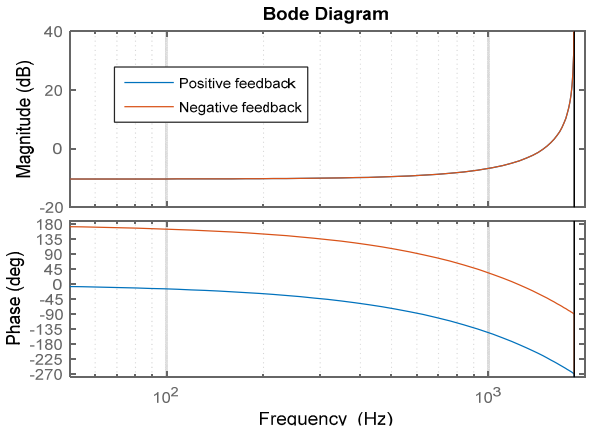

FIGURE 11. Bode diagram of the open-loop transfer function for proportional feedback of the capacitor voltage.

The Bode plot of the open-loop transfer function for $f_r = f_s/2$, $L(z)$, is represented in Fig. 11 for positive ($K_v > 0$) and negative ($K_v < 0$) feedbacks. Focusing on the figure for the Nyquist frequency, it seems that there are no crossings with $-180°$. However, to correctly determine C_N, Table 1 must be applied taking into account that $l = 1$. Parameter K_N is required which, from its definition and (29), can be obtained as

$$K_N = -K_v \cdot \frac{2L_2}{L_1 + L_2}. \quad (32)$$

Using this equation and Table 1, it is clear that negative feedback ($K_v < 0$) leads to $K_N > 0$, $C_N = -1$, and the control will be unstable independently of other possible crossings. In contrast, positive feedback ($K_v > 0$) leads to $K_N < 0$ and $C_N = 0$, meaning that the control will be stable given that the remaining parameters are zero, that is $C^- = 0$ and $C_0 = 0$.

For $K_v > 0$, C_0 can be obtained from Table 2. Since there are no poles at z $= 1$, i.e. $k = 0$, and $K_0 > 0$, C_0 is always 0. Concerning C^-, Fig. 11 shows that there is one crossing with $-180°$, which must be counted if the gain is higher than 1 (higher than 0 dB). Applying (30) reveals that this crossing is at $f = f_s/3$. As a result, using (29), the open-loop gain and the condition to achieve $C^- = 0$ are

$$\left|L(e^{j2\pi/3})\right| = K_v \cdot \frac{2L_2}{L_1 + L_2} < 1 \Rightarrow K_{v,\max} = \frac{L_1 + L_2}{2L_2}. \quad (33)$$

The conclusions about the stability analysis with proportional feedback of the capacitor voltage for $f_r = f_s/2$ are summarized in Table 6. The condition for stable damping is the application of positive feedback ($K_v > 0$) with a gain that meets constraint (33). It is worth noting that the use of the existing Bode stability criteria instead of the proposed DGBC would have led to incorrect conclusions about stability since the crossings at ω_N are not detected. Specifically, the existing Bode stability criteria would have concluded that active damping can also be achieved with negative feedback ($K_v < 0$), which has been shown to be incorrect.

TABLE 6. Stability analysis for active damping with proportional feedback of the capacitor voltage.

Case	$f_r = f_s/2$	
$K_v < 0$ $C_N = -1$ $C^- = 0$	$\lvert K_v\rvert < (L_1+L_2)/L_2$ $C_0 = 0$, **Z = 1**	$\lvert K_v\rvert > (L_1+L_2)/L_2$ $C_0 = -1$, **Z = 2**
$K_v > 0$ $C_N = 0$ $C_0 = 0$	$K_v < (L_1+L_2)/2L_2$ $C^- = 0$, **Z = 0**	$K_v > (L_1+L_2)/2L_2$ $C^- = 1$, **Z = 2**

TABLE 7. System parameters used for the validation.

System parameters	
$L_1 = 2.44$ mH	$r_{L1} = 108$ mΩ
$L_2 = 1.03$ mH	$r_{L2} = 68$ mΩ
$C = 10$ µF	DC voltage $V_{dc} = 200$ V
Crossover frequency of the current control, $f_c = 150$ Hz	Cutoff frequency of the current filter, $f_{c,i1} = 1060$ Hz
Active damping with i_c	Active damping with v_c
Switching and sampling frequencies $f_s = 5000$ Hz	Switching and sampling frequencies $f_s = 3700$ Hz
$f_r = f_s/2.67$	$f_r = f_s/1.98$

IV. VALIDATION OF THE DGBC CASE-STUDY

A. ROOT LOCUS

The two active damping methods presented in the previous section (see Fig. 5 and Fig. 8) are analyzed here for the system parameters shown in Table 7. In both cases, the converter-side current is regulated by using a proportional controller designed to achieve a crossover frequency $f_c = 150$ Hz, and the measured current is filtered with an analog filter with a low cutoff frequency $f_{c,i1} = 1060$ Hz.

It has been shown that the active damping action, analyzed in section III, makes it possible to mitigate the resonance. However, when including afterwards the current controller, setting a high cross-over frequency can modify the stability margins of the active damping. Thus, for the validation of the case-study, the values of f_c and $f_{c,i1}$ are selected relatively small so that the current controller hardly affects the performance of the active damping.

For active damping with capacitor current feedback, the switching and sampling frequencies are set to 5000 Hz. Since $f_r = f_s/2.67 > f_s/6$, the damping constant K_d must be negative for a stable control. Furthermore, from the DGBC stability criterion, summarized in Table 5, its absolute value must be lower than $|K_{d,max,C-}| = 96.9$ (see (21)) to avoid C^- crossings, and also lower than $|K_{d,max,Cn}| = 12.0$ (see (23)) to avoid C_N crossings. Thus, $-12.0 < K_d < 0$ defines the stable region whereas $-96.9 < K_d < -12.0$ results in one unstable closed-loop pole, $Z = 2 \cdot C^- - C_N = 0 - (-1) = 1$, and $K_d < -96.9$ leads to three unstable closed-loop poles, $Z = 2 \cdot C^- - C_N = 2 - (-1) = 3$.

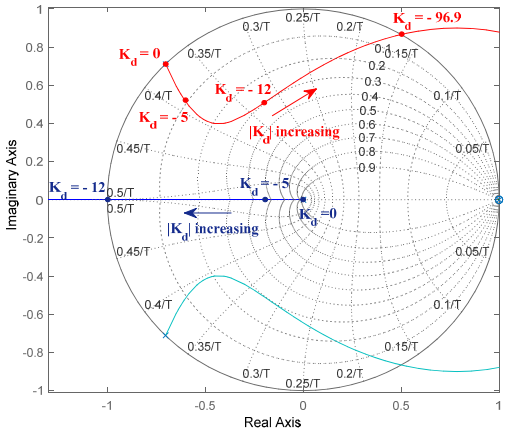

FIGURE 12. Root locus for active damping with negative capacitor current feedback ($f_r = f_s/2.67$).

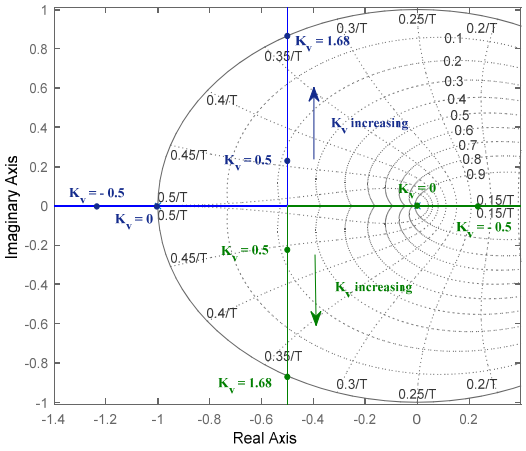

FIGURE 13. Root locus for active damping with capacitor voltage feedback ($f_r = f_s/2$).

These results are confirmed by the root locus applied to (15), shown in Fig. 12. In this figure, it can be observed that three poles appear, two being due to the LCL filter resonance and one to the discretization. For $K_d = 0$, the original filter resonance is not damped whereas setting $K_d = -5$ successfully provides active damping. As $|K_d|$ continues to increase, the filter resonance remains well damped up to very high values, and the poles go outside the unit circle for $K_d < -96.9$. This was predicted by the DGBC but also by the continuous GBC due to the $-180°$ crossing in the Bode plot at a positive frequency $0 < f < f_s/2$. Concerning the pole due to discretization, its damping rapidly decreases, and it becomes unstable as soon as $K_d < -12.0$. The appearance of this instability was predicted by the DGBC due to the $-180°$ crossing at the Nyquist frequency $f = f_s/2$. However, none of the existing Bode criteria considers this crossing, which may result in an unstable response of the active damping.

For active damping with capacitor voltage feedback, the switching and sampling frequencies are set to 3700 Hz and thus $f_r = f_s/1.98 \approx f_s/2$. From the DGBC stability criterion, summarized in Table 6, the stable region is defined by $0 < K_v < 1.68$. On the contrary, $-3.37 < K_v < 0$ results

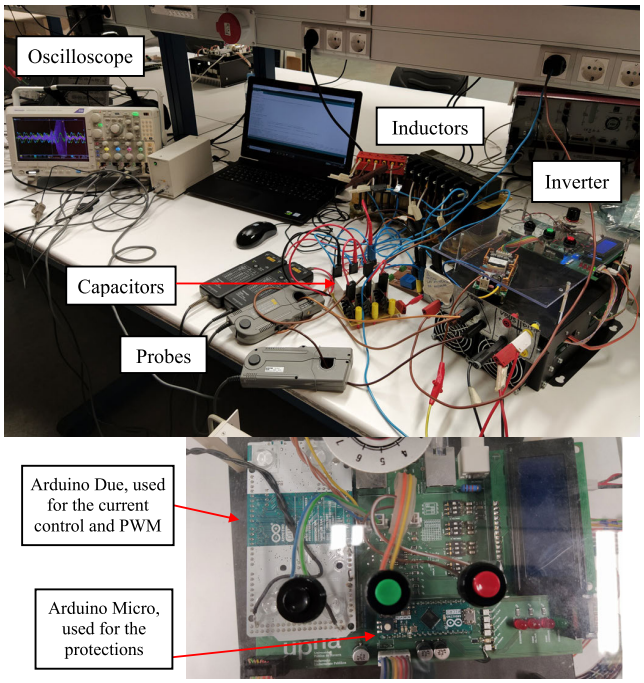

FIGURE 14. Experimental setup.

in one unstable closed-loop pole, $Z = 2{\cdot}C^{-} - C_N = 0 - (-1) = 1$, while $K_v > 1.68$ leads to two unstable closed-loop poles, $Z = 2{\cdot}C^{-} - C_N = 2 - 0 = 2$.

These results are validated by the root locus applied to (29), shown in Fig. 13. As can be observed, setting $K_v < 0$ always results in one pole outside the unit circle, which was predicted by the proposed DGBC due to the $-180°$ crossing at the Nyquist frequency $f = f_s/2$. However, this crossing is not visible in the Bode plot and thus this pole is not detected by the existing Bode criteria. For $0 < K_v < 1.68$, both poles are inside the unit circle, first in the real axis and then they become complex. Finally, both poles again become unstable for $K_v > 1.68$.

It is worth noting that the root locus is convenient for the validation since only one parameter alters, in this case the damping constant. However, using this tool for the controller design when two or more parameters change becomes complicated. Contrariwise, in section III, the DGBC has been shown to be intuitive for the design when two or three parameters change, specifically the damping constant, the frequencies ratio f_s/f_r and the controller parameter r.

B. EXPERIMENTAL RESULTS

Figure 14 shows the setup used for the experimental validation at the top, and a zoom of the control board at the bottom. The setup comprises a three-phase inverter connected to an LCL filter and then short-circuited. Although the test platform is not connected to the grid, the results are extensible to a grid-connected system since the grid voltage is a disturbance and has no influence on the stability analysis. The converter-side current control, together with the two active

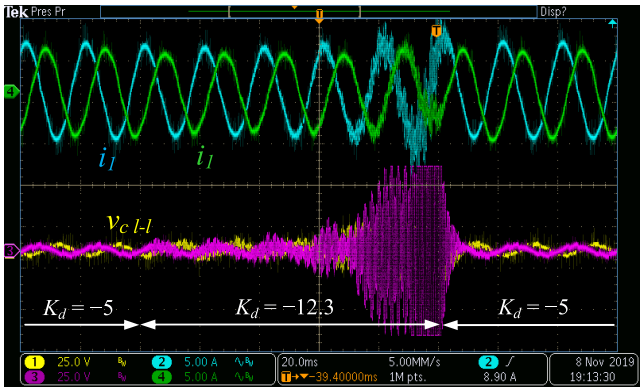

FIGURE 15. Experimental results for active damping with proportional feedback of the capacitor current ($f_r = f_s/2.67$).

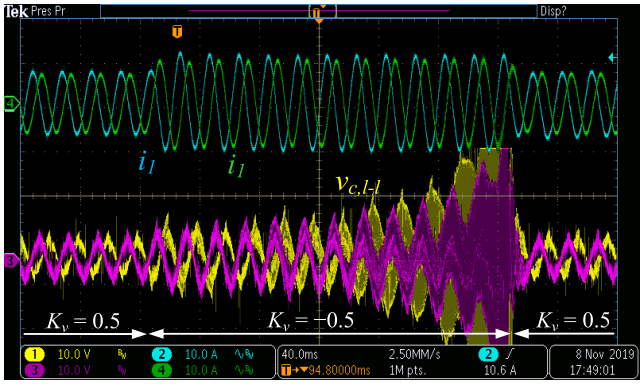

FIGURE 16. Experimental results for active damping with proportional feedback of the capacitor voltage ($f_r = f_s/1.98$).

damping methods, as described above (see Fig. 5 and Fig. 10), are implemented in the Arduino Due. The control board also includes an Arduino Micro where the converter protections are executed. The oscilloscope is a Tektronix MDO3054, with a bandwidth of 500 MHz and a sampling rate of 2.5 GS/s. The current probes are two Yokogawa 701930, with a bandwidth of 10 MHz, and the voltage differential probes are two Tektronix P5200, with a bandwidth of 50 MHz. The system parameters are the same as previously, as shown in Table 7.

Figure 15 shows the experimental results for active damping with proportional feedback of the capacitor current when $f_r = f_s/2.67$, where the represented variables are two converter-side currents and two line-to-line capacitor voltages. At the beginning, the damping constant K_d is set to -5, and a stable and well-damped control is achieved. Then, K_d is modified to -12.3, which causes the system to become unstable. The oscillation is at the Nyquist frequency, i.e. $f = f_s/2 = 2500$ Hz. This is in accordance with the DGBC analysis, which predicted the appearance of one unstable pole for $K_d < -12$ due to the $-180°$ crossing at the Nyquist frequency. Finally, K_d is again set to -5, resulting in a damped response.

Figure 16 shows the experimental results for active damping with proportional feedback of the capacitor voltage when $f_r = f_s/1.98 \approx f_s/2$, where the same variables are represented. Similarly to the previous case, first the control is damped and

stable for $K_v = 0.5$, it becomes unstable for $K_v = -0.5$, and then it is stabilized for $K_v = 0.5$. The oscillation is again at the Nyquist frequency, in this case $f = f_s/2 = 1850$ Hz. This was expected thanks to the DGBC analysis, which detected the appearance of one unstable pole for $K_v < 0$ due to the $-180°$ crossing at the Nyquist frequency.

V. CONCLUSION

This article proposes a new stability criterion for discrete systems, called DGBC, which combines the advantages of the Nyquist and Bode criteria. As it uses information from the open-loop Bode plot, the DGBC is easy to apply and can provide clear guidelines about the controller design. At the same time, since it is based on the Nyquist criterion, it is applicable under any conditions, unlike the existing Bode criteria.

For the formulation of the DGBC, particular attention is paid to what occurs at 0 Hz and the Nyquist frequency, as this information is not visible in the Bode plot and it is very important for the stability of discrete systems.

As a case-study, the proposed method is applied to determine the stability and provide design guidelines for the active damping of an inverter with LCL filter. First, the active damping with capacitor current feedback is analyzed, which corresponds to an open-loop with no poles at z $= -1$. Then, the active damping with capacitor voltage feedback when $f_r = f_s/2$ is studied, which corresponds to an open-loop with one pole at z $= -1$. For both cases, and in contrast to the existing Bode criteria, the DGBC is able to accurately obtain the stability region, including the oscillation which appears at the Nyquist frequency. These conclusions are validated through experimental results performed with a three-phase inverter and an LCL filter.

REFERENCES

[1] A. Zervos *et al.* (2020). *Renewables 2020 Global Status Report*. Paris, France: REN 21 Secretariat. [Online]. Available: https://www.ren21.net/wp-content/uploads/2019/05/gsr_2020_full_report_en.pdf

[2] B. Burger *et al.* (Sep. 2020). *Photovoltaics Report*. Fraunhofer Institute for Solar Energy Systems (ISE). [Online]. Available: https://www.ise.fraunhofer.de/content/dam/ise/de/documents/publications/studies/Photovoltaics-Report.pdf

[3] I. Komusanak *et al.* (Feb. 2020). *Wind Energy in Europe in 2019: Trends and Statistics*. Wind Europe. [Online]. Available: https://windeurope.org/wp-content/uploads/files/about-wind/statistics/WindEurope-Annual-Statistics-2019.pdf

[4] S. Dawn, P. K. Tiwari, and A. K. Goswami, "An approach for long term economic operations of competitive power market by optimal combined scheduling of wind turbines and FACTS controllers," *Energy*, vol. 181, pp. 709–723, Aug. 2019.

[5] R. K. Varma and E. M. Siavashi, "Enhancement of solar farm connectivity with smart PV inverter PV-STATCOM," *IEEE Trans. Sustain. Energy*, vol. 10, no. 3, pp. 1161–1171, Jul. 2019.

[6] A. Urtasun, J. Samanes, E. L. Barrios, P. Sanchis, and L. Marroyo, "Control of a photovoltaic array interfacing current-mode-controlled boost converter based on virtual impedance emulation," *IEEE Trans. Ind. Electron.*, vol. 66, no. 5, pp. 3496–3506, May 2019.

[7] M. Sitbon, S. Schacham, T. Suntio, and A. Kuperman, "Improved adaptive input voltage control of a solar array interfacing current mode controlled boost power stage," *Energy Convers. Manage.*, vol. 98, pp. 369–375, Jul. 2015.

[8] W. Wu, J. Ji, and F. Blaabjerg, "Aalborg inverter—A new type of 'buck in buck, boost in boost' grid-tied inverter," *IEEE Trans. Power Electron.*, vol. 30, no. 9, pp. 4784–4793, Sep. 2015.

[9] D. Elizondo and A. Urtasun, "Dual-mode soft-transition control for single-phase grid-connected photovoltaic inverters," in *Proc. IEEE 19th Workshop Control Model. Power Electron. (COMPEL)*, Padua, Italy, Jun. 2018, pp. 1–6.

[10] M. R. Islam, A. M. Mahfuz-Ur-Rahman, K. M. Muttaqi, and D. Sutanto, "State-of-the-art of the medium-voltage power converter technologies for grid integration of solar photovoltaic power plants," *IEEE Trans. Energy Convers.*, vol. 34, no. 1, pp. 372–384, Mar. 2019.

[11] C. G. Dincan, P. Kjaer, Y.-H. Chen, E. Sarra-Macia, S. Munk-Nielsen, C. L. Bak, and S. Vaisambhayana, "Design of a high-power resonant converter for DC wind turbines," *IEEE Trans. Power Electron.*, vol. 34, no. 7, pp. 6136–6154, Jul. 2019.

[12] A. Urtasun and D. D.-C. Lu, "Control of a single-switch two-input buck converter for MPPT of two PV strings," *IEEE Trans. Ind. Electron.*, vol. 62, no. 11, pp. 7051–7060, Nov. 2015.

[13] A. K. Yadav, K. Gopakumar, K. R. R. L. Umanand, S. Bhattacharya, and W. Jarzyna, "A hybrid 7-level inverter using low-voltage devices and operation with single DC-link," *IEEE Trans. Power Electron.*, vol. 34, no. 10, pp. 9844–9853, Oct. 2019.

[14] P. Guo, Q. Xu, Y. Yue, F. Ma, Z. He, A. Luo, and J. M. Guerrero, "Analysis and control of modular multilevel converter with split energy storage for railway traction power conditioner," *IEEE Trans. Power Electron.*, vol. 35, no. 2, pp. 1239–1255, Feb. 2020.

[15] Z. Xin, P. C. Loh, X. Wang, F. Blaabjerg, and Y. Tang, "Highly accurate derivatives for LCL-filtered grid converter with capacitor voltage active damping," *IEEE Trans. Power Electron.*, vol. 31, no. 5, pp. 3612–3625, May 2016.

[16] A. G. Yepes, F. D. Freijedo, J. Doval-Gandoy, Ó. López, J. Malvar, and P. Fernandez-Comesaña, "Effects of discretization methods on the performance of resonant controllers," *IEEE Trans. Power Electron.*, vol. 25, no. 7, pp. 1692–1712, Jul. 2010.

[17] G. F. Franklin, J. D. Powell, M. Workman, *Digital Control of Dynamic Systems*, 3rd ed. Reading, MA, USA: Addison-Wesley Longman, 1998.

[18] J. L. Agorreta, M. Borrega, J. López, and L. Marroyo, "Modeling and control of *N*-paralleled grid-connected inverters with LCL filter coupled due to grid impedance in PV plants," *IEEE Trans. Power Electron.*, vol. 26, no. 3, pp. 770–785, Mar. 2011.

[19] J. Samanes and E. Gubia, "Sensorless active damping strategy for parallel interleaved voltage source power converters with LCL filter," in *Proc. IEEE Appl. Power Electron. Conf. Exposit. (APEC)*, Tampa, FL, USA, Mar. 2017, pp. 3632–3639.

[20] J. Dannehl, F. W. Fuchs, S. Hansen, and P. B. Thøgersen, "Investigation of active damping approaches for PI-based current control of grid-connected pulse width modulation converters with LCL filters," *IEEE Trans. Ind. Appl.*, vol. 46, no. 4, pp. 1509–1517, Jul. 2010.

[21] A. Urtasun, P. Sanchis, F. Guinjoan, and L. Marroyo, "Parameter-independent battery control based on series and parallel impedance emulation," *IEEE Access*, vol. 7, pp. 70021–70031, Jun. 2019.

[22] X. Li, X. Wu, Y. Geng, X. Yuan, C. Xia, and X. Zhang, "Wide damping region for LCL-type grid-connected inverter with an improved capacitor-current-feedback method," *IEEE Trans. Power Electron.*, vol. 30, no. 9, pp. 5247–5259, Sep. 2015.

[23] X. Wu, G. Xiao, and B. Lei, "Simplified discrete-time modeling for convenient stability prediction and digital control design," *IEEE Trans. Power Electron.*, vol. 28, no. 11, pp. 5333–5342, Nov. 2013.

[24] R. Pena-Alzola, M. Liserre, F. Blaabjerg, M. Ordonez, and Y. Yang, "LCL-filter design for robust active damping in grid-connected converters," *IEEE Trans. Ind. Informat.*, vol. 10, no. 4, pp. 2192–2203, Nov. 2014.

[25] R. Pena-Alzola, J. Roldan-Perez, E. Bueno, F. Huerta, D. Campos-Gaona, M. Liserre, and G. Burt, "Robust active damping in LCL-filter-based medium-voltage parallel grid inverters for wind turbines," *IEEE Trans. Power Electron.*, vol. 33, no. 12, pp. 10846–10857, Dec. 2018.

[26] Y. Tang, W. Yao, P. C. Loh, and F. Blaabjerg, "Design of LCL filters with LCL resonance frequencies beyond the Nyquist frequency for grid-connected converters," *IEEE J. Emerg. Sel. Topics Power Electron.*, vol. 4, no. 1, pp. 3–14, Mar. 2016.

[27] G. Gohil, L. Bede, R. Teodorescu, T. Kerekes, and F. Blaabjerg, "Line filter design of parallel interleaved VSCs for high-power wind energy conversion systems," *IEEE Trans. Power Electron.*, vol. 30, no. 12, pp. 6775–6790, Dec. 2015.

[28] J. Samanes, A. Urtasun, E. Gubia, and A. Petri, "Robust multisampled capacitor voltage active damping for grid-connected power converters," *Int. J. Electr. Power Energy Syst.*, vol. 105, pp. 741–752, Feb. 2019.

[29] W. Lenwari, M. Sumner, and P. Zanchetta, "The use of genetic algorithms for the design of resonant compensators for active filters," *IEEE Trans. Ind. Electron.*, vol. 56, no. 8, pp. 2852–2861, Aug. 2009.

[30] P. S. Sanjan, N. Gowtham, M. S. Bhaskar, U. Subramaniam, D. J. Almakhles, S. Padmanaban, and N. G. Yamini, "Enhancement of power quality in domestic loads using harmonic filters," *IEEE Access*, vol. 8, pp. 197730–197744, Oct. 2020.

[31] A. Javadi, M. Abarzadeh, L.-A. Gregoire, and K. Al-Haddad, "Real-time HIL implementation of a single-phase distribution level THSeAF based on D-NPC converter using proportional-resonant controller for power quality platform," *IEEE Access*, vol. 7, pp. 110372–110386, Aug. 2019.

[32] D. Arricibita, P. Sanchis, R. Gonzalez, and L. Marroyo, "Impedance emulation for voltage harmonic compensation in PWM stand-alone inverters," *IEEE Trans. Energy Convers.*, vol. 32, no. 4, pp. 1335–1344, Dec. 2017.

[33] G. Escobar, M. Hernandez-Gomez, A. A. Valdez-Fernandez, M. J. Lopez-Sanchez, and G. A. Catzin-Contreras, "Implementation of a $6n \pm 1$ repetitive controller subject to fractional delays," *IEEE Trans. Ind. Electron.*, vol. 62, no. 1, pp. 444–452, Jan. 2015.

[34] C. K. Lam, M. T. Tan, S. M. Cox, and K. S. Yeo, "Class-D amplifier power stage with PWM feedback loop," *IEEE Trans. Power Electron.*, vol. 28, no. 8, pp. 3870–3881, Aug. 2013.

[35] R. Ren, F. Zhang, B. Liu, F. Wang, Z. Chen, and J. Wu, "A closed-loop modulation scheme for duty cycle compensation of PWM voltage distortion at high switching frequency inverter," *IEEE Trans. Ind. Electron.*, vol. 67, no. 2, pp. 1475–1486, Feb. 2020.

[36] J. Yuan, Z. Zhao, B. Chen, C. Li, J. Wang, C. Tian, and Y. Chen, "An immune-algorithm-based dead-time elimination PWM control strategy in a single-phase inverter," *IEEE Trans. Power Electron.*, vol. 30, no. 7, pp. 3964–3975, Jul. 2015.

[37] A. Guha and G. Narayanan, "Impact of dead time on inverter input current, DC-link dynamics, and light-load instability in rectifier-inverter-fed induction motor drives," *IEEE Trans. Ind. Appl.*, vol. 54, no. 2, pp. 1414–1424, Mar./Apr. 2018.

[38] G. Zhou, G. Mao, H. Zhao, W. Zhang, and S. Xu, "Digital average voltage/digital average current predictive control for switching DC–DC converters," *IEEE J. Emerg. Sel. Topics Power Electron.*, vol. 6, no. 4, pp. 1819–1830, Dec. 2018.

[39] G. Zhou, G. Mao, S. Zhou, Z. Li, and M. Leng, "Digital valley v2 control for boost converter with fast load-transient performance," *IEEE Trans. Circuits Syst. II, Exp. Briefs*, vol. 67, no. 10, pp. 2089–2093, Oct. 2020.

[40] W.-C. Chen, C.-C. Chen, C.-Y. Yao, and R.-J. Yang, "A fast-transient wide-voltage-range digital-controlled buck converter with cycle-controlled DPWM," *IEEE Trans. Very Large Scale Integr. (VLSI) Syst.*, vol. 24, no. 1, pp. 17–25, Jan. 2016.

[41] R. Maheshwari, I. Trintis, L. Torok, S. Munk-Nielsen, P. J. Douglass, and L. Bede, "A novel high bandwidth current control strategy for SiC MOSFET based active front-end rectifiers under unbalanced input voltage conditions," *IEEE Trans. Ind. Electron.*, vol. 64, no. 10, pp. 8310–8320, Oct. 2017.

[42] Y. Cai, Y. He, H. Zhou, and J. Liu, "Active damping disturbance rejection control strategy of LCL grid-connected inverter based on inverter-side current feedback," *IEEE J. Emerg. Sel. Topics Power Electron.*, early access, Aug. 18, 2020, doi: 10.1109/JESTPE.2020.3017678.

[43] W. Yao, Y. Yang, X. Zhang, F. Blaabjerg, and P. C. Loh, "Design and analysis of robust active damping for LCL filters using digital notch filters," *IEEE Trans. Power Electron.*, vol. 32, no. 3, pp. 2360–2375, Mar. 2017.

[44] D. Perez-Estevez, J. Doval-Gandoy, A. G. Yepes, O. Lopez, and F. Baneira, "Enhanced resonant current controller for grid-connected converters with LCL filter," *IEEE Trans. Power Electron.*, vol. 33, no. 5, pp. 3765–3778, May 2018.

[45] J. S. Mills, "Use of Ragazzini method to design idle speed control algorithms," in *Proc. IEE Colloq. Power Train Control*, London, U.K., May 1990, pp. 4-1–4-5.

[46] A. G. Yepes, F. D. Freijedo, O. Lopez, and J. Doval-Gandoy, "Analysis and design of resonant current controllers for voltage-source converters by means of Nyquist diagrams and sensitivity function," *IEEE Trans. Ind. Electron.*, vol. 58, no. 11, pp. 5231–5250, Nov. 2011.

[47] J. Yin, S. Duan, and B. Liu, "Stability analysis of grid-connected inverter with LCL filter adopting a digital single-loop controller with inherent damping characteristic," *IEEE Trans. Ind. Informat.*, vol. 9, no. 2, pp. 1104–1112, May 2013.

[48] K. Nakamura, K. Yubai, D. Yashiro, and S. Komada, "Controller design method achieving maximization of control bandwidth by using Nyquist diagram," in *Proc. Int. Autom. Control Conf. (CACS)*, Taichung, Taiwan, Nov. 2016, pp. 35–40.

[49] Y. Liao and X. Wang, "General rules of using bode plots for impedance-based stability analysis," in *Proc. IEEE 19th Workshop Control Model. Power Electron. (COMPEL)*, Padua, Italy, Jun. 2018, pp. 1–6.

[50] R. Ridley. *Loop Bode Plots and Nyquist Diagrams*. Ridley Engineering Design Center. Accessed: Oct. 2018. [Online]. Available: https://ridleyengineering.com/design-center-ridley-engineering/41-frequency-response/142-078-loop-bode-plots-and-nyquist-diagrams.html

[51] M. Herdin and M. Sonst, "A brief how to: Analyzing control loop stability with bode plots using modern oscilloscopes," *Bodo's Power Syst.*, pp. 32–34, Jan. 2020.

[52] J. Dannehl, M. Liserre, and F. W. Fuchs, "Filter-based active damping of voltage source converters with *LCL* filter," *IEEE Trans. Ind. Electron.*, vol. 58, no. 8, pp. 3623–3633, Aug. 2011.

[53] J. Hahn, T. Edison, and T. F. Edgar, "A note on stability analysis using Bode plots," *Chem. Eng. Educ.*, vol. 35, no. 3, pp. 208–211, 2001.

[54] H. Unbehauen, *Regelungstechnik I: Klassische Verfahren Zur Analyse Und Synthese Linearer Kontinuierlicher Regelsysteme, Fuzzy-Regelsysteme*. Berlin, Germany: Springer, 1992.

[55] D. Lumbreras, E. L. Barrios, A. Ursua, L. Marroyo, and P. Sanchis, "On the stability criteria for inverter current control loops with LCL output filters and varying grid impedance," in *Proc. 19th Eur. Conf. Power Electron. Appl. (EPE ECCE Europe)*, Warsaw, Poland, Sep. 2017, pp. 1–10.

[56] D. Lumbreras, E. L. Barrios, A. Urtasun, A. Ursua, L. Marroyo, and P. Sanchis, "On the stability of advanced power electronic converters: The generalized bode criterion," *IEEE Trans. Power Electron.*, vol. 34, no. 9, pp. 9247–9262, Sep. 2019.

[57] M. Vidyasagar, R. K. Bertschmann, and C. S. Sallaberger, "Some simplifications of the graphical Nyquist criterion," *IEEE Trans. Autom. Control*, vol. 33, no. 3, pp. 301–305, Mar. 1988.

[58] J. Samanes, A. Urtasun, E. L. Barrios, D. Lumbreras, J. Lopez, E. Gubia, and P. Sanchis, "Control design and stability analysis of power converters: The MIMO generalized bode criterion," *IEEE J. Emerg. Sel. Topics Power Electron.*, vol. 8, no. 2, pp. 1880–1893, Jun. 2020.

[59] C. Bao, X. Ruan, X. Wang, W. Li, D. Pan, and K. Weng, "Step-by-step controller design for LCL-type grid-connected inverter with capacitor–current-feedback active-damping," *IEEE Trans. Power Electron.*, vol. 29, no. 3, pp. 1239–1253, Mar. 2014.

[60] A. Urtasun, P. Sanchis, and L. Marroyo, "DC capacitance reduction in three-phase photovoltaic inverters by using virtual impedance emulation," in *Proc. 21st Eur. Conf. Power Electron. Appl. (EPE)*, Genova, Italy, Sep. 2019, pp. 1–9.

ANDONI URTASUN (Senior Member, IEEE) was born in Pamplona, Spain, in 1987. He received the M.Sc. degree in electrical engineering from the Public University of Navarre (UPNA), Pamplona, in 2010, and the M.Sc. degree from the Institut National Polytechnique de Toulouse, Toulouse, France, in 2010, and the Ph.D. degree in electrical engineering from UPNA in 2015.

In 2010, he joined the Electrical Engineering, Power Electronics and Renewable Energy Research Group, UPNA, where he is currently an Associate Professor. He has been involved in more than 15 research projects, mainly in cooperation with industry. He has coauthored more than 30 articles in international journals and conferences. His research interests include power electronics and renewable energies.

JAVIER SAMANES (Member, IEEE) was born in Pamplona, Spain, in 1990. He received the M.Sc. degree in electrical engineering, the M.Sc. degree in renewable energy engineering, and the Ph.D. degree in electrical engineering from the Public University of Navarre (UPNA), Pamplona, in 2014, 2016, and 2018, respectively.

In 2014, he joined the Electrical Engineering, Power Electronics and Renewable Energy Research Group, UPNA, where he is currently an Assistant Professor and a member of the Institute of Smart Cities. In 2018, he was a Visiting Scholar with the Center for Power Electronic Systems, Virginia Tech, USA. His research interests include power electronics and renewable energies.

ERNESTO L. BARRIOS (Member, IEEE) was born in Pamplona, Spain, in 1988. He received the B.Sc., M.Sc., and Ph.D. degrees in electrical engineering from the Public University of Navarre (UPNA), Pamplona, in 2009, 2012 and 2015, respectively.

In 2011, he joined the Electrical Engineering, Power Electronics and Renewable Energy Research Group, Public University of Navarre, where he is currently an Associate Professor. His main research interests include high-frequency magnetics, wide-bandgap power semiconductor devices and power converters for renewable energies, particularly for photovoltaics and fuel cells.

PABLO SANCHIS (Senior Member, IEEE) received the M.Sc. degree in management and business administration and the M.Sc. and Ph.D. degrees in electrical engineering from the Public University of Navarre (UPNA), Pamplona, Spain, in 1994, 1995, and 2002, respectively.

From 1996 to 1998, he was a Guest Researcher with the Delft University of Technology, The Netherlands. In 1998, he joined the Department of Electrical, Electronic and Communications Engineering, UPNA, where he is currently an Associate Professor. He was the Vice Dean of the School of Industrial and Telecommunications Engineering. He is also the Director of the UPNA Chair for Renewable Energies and the Director of the Research Resources and Structures Unit, UPNA.

He has been involved in more than 70 research projects both with public funding and in co-operation with industry. He has co-invented eight patents. He has also coauthored more than 140 articles and contributions in international journals and conferences. He has supervised nine Ph.D. theses. His research interests include renewable energies, power electronics, electric energy storage technologies, grid integration of renewable energies, and electric microgrids. In 2013, he received the UPNA Research Award for the Best Technical Paper and the UPNA Excellence in Teaching Award in 2017.